

Diffraction casting

Ryosuke Mashiko^a, Makoto Naruse^{a,b}, Ryoichi Horisaki^{a,*}

^aThe University of Tokyo, Graduate School of Information Science and Technology, Department of Information Physics and Computing, 7-3-1 Hongo, Bunkyo-ku, Tokyo, Japan, 113-8656

^bDeceased.

Abstract. Optical computing is considered a promising solution for the growing demand for parallel computing in various cutting-edge fields, requiring high integration and high speed computational capacity. In this paper, we propose a novel optical computation architecture called diffraction casting (DC) for flexible and scalable parallel logic operations. In DC, a diffractive neural network (DNN) is designed for single instruction, multiple data (SIMD) operations. This approach allows for the alteration of logic operations simply by changing the illumination patterns. Furthermore, it eliminates the need for encoding and decoding the input and output, respectively, by introducing a buffer around the input area, facilitating end-to-end all-optical computing. We numerically demonstrate DC by performing all 16 logic operations on two arbitrary 256 bits parallel binary inputs. Additionally, we showcase several distinctive attributes inherent in DC, such as the benefit of cohesively designing the diffractive elements for SIMD logic operations, assuring high scalability and integration capability. Our study offers a novel design architecture for optical computers and paves the way for a next-generation optical computing paradigm.

Keywords: optical computing, diffractive neural network, SIMD operations, parallel computing, logic operations, machine learning.

*Ryoichi Horisaki, horisaki@g.ecc.u-tokyo.ac.jp

1 Introduction

Optical computing is a longstanding and captivating topic in the fields of optics and photonics. It is considered a potential post-Moore computing technology,¹ offering distinct advantages including high bandwidth, rapid processing speed, low power consumption, and parallelism.^{2,3} Around the 1980s, optical computing was actively explored, with developments in technologies such as optical vector matrix multipliers⁴⁻⁷ and optical associative memories.⁸⁻¹⁰ Among these, shadow casting (SC) emerged as a prominent optical computing technology of that era.¹¹⁻¹⁴ SC facilitated single instruction, multiple data (SIMD) for logical operations through optical and spatially parallel computing. The SC scheme relied on shadowgrams, which optically generated a single output image through massively parallel logic operations from two binary input images. The versatility of SIMD logic operations was attained by altering the illumination pattern of the shadowgrams.

Another key aspect involved the computational encoding and decoding of input and output images, respectively, designed to balance light intensities between the zeros and ones in the binary images. This computational process was an obstacle in achieving end-to-end optical computing. Despite the anticipated benefits in speed and energy efficiency, these optical computing technologies in the 1980s stagnated due to limitations in hardware (fabrication) and software (design) for optical components at that time. As a result, they lagged behind the major progress in electronic computing.

Over the past few decades, significant advancements in microfabrication, mathematical optimization, and computational power have dramatically transformed the field of optical computing from what it was in the 1980s. Several pioneering optical computing techniques have been studied, including waveguide-based photonic circuits and diffractive neural networks (DNNs). Waveguide-based photonic circuits, which integrate waveguide interferometers, have high compatibility with currently existing electrical computers and circuits. They have led to a wide range of applications, such as vector-matrix operations,^{15–17} logical operations,^{18–24} and integrated reconfigurable circuits.^{25–27}

DNNs consist of cascaded diffractive optical elements (DOEs), which emulate neural network connections as light waves pass through the DOEs. This configuration utilizes the spatial parallelism of light and realizes fast and energy-efficient computation. Extensive and attractive applications based on DNNs have been proposed, including image classification,^{28–31} image processing,^{32–34} linear transformations^{35–37} and logic operations.^{38–42}

Currently, the demand for computation in SIMD logic operations has intensified, particularly due to advancements in cutting-edge technologies such as image processing, machine learning, and blockchain.^{43–45} Traditional computation with central processing units (CPUs) is often in-

adequate to meet the computational needs of these fields. Consequently, graphics processing units (GPUs),⁴⁶ tensor processing units (TPUs),⁴⁷ field-programmable gate arrays (FPGAs),^{48,49} and application-specific integrated circuits (ASICs)^{50,51} are employed as SIMD-specific devices. The trend towards high-speed, energy-efficient, and massively parallel computing aligns well with the advantages of optical computation. As a result, there is a rapid increase in efforts to develop practical optical computing methods for SIMD logic operations. Optical SIMD logic operations have been achieved using waveguide photonic circuits.^{26,27} However, a drawback of this approach is its limited scalability, which arises from the need for precise yet large-scale fabrication. The use of DNNs holds potential as a solution to this issue, owing to the parallelism inherent in free-space propagation. For instance, several types of DNN-based logic operations have been proposed to overcome this drawback,^{38–42} but the realization of SIMD logic operations using DNNs remains unachieved. Moreover, these methods still require computational encoding and decoding of the input and output, respectively, posing a significant challenge toward end-to-end optical computing, similarly to the SC scheme.

In this study, considering the background mentioned above, we present a method termed diffraction casting (DC) for conducting optical SIMD logic operations by incorporating the SC scheme and DNNs. DC revives SC through the use of DNNs. Therefore, DC shares the motivation of SC but exhibits several differences and advantages over SC. Unlike SC, which is based on geometrical optics, DC is grounded in wave optics. As a result, DC incorporates wave phenomena such as diffraction and interference through the use of DOE cascades in DNNs, and is anticipated to offer greater integration capability compared to SC. Another advantage of DC is its elimination of the need for computational encoding and decoding of the input and output, respectively, which have been inherent bottlenecks in the SC scheme and previous DNN-based logic operations re-

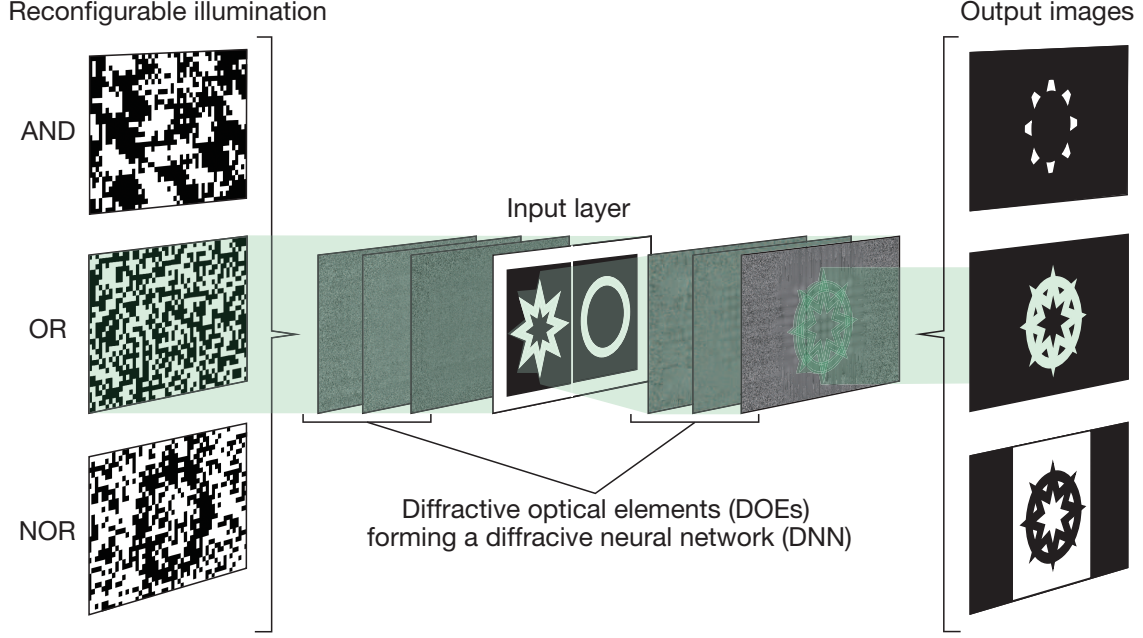


Fig 1 Schematic diagram of diffraction casting (DC). The selection of a logic operation is performed using reconfigurable illumination without any modification to the optical hardware.

ferred to above. This is enabled by introducing a buffer area around the input pair. In the rest of the paper, we will elaborate on the architectural design of DC, including the forward model, the optimization process, and provide numerical demonstrations.

2 Materials and Methods

2.1 Concept of Diffraction Casting

DC is designed for 16 types of SIMD logic operations, processing two input binary images to produce one output binary image. Figure 1 depicts the conceptual architecture of DC. DC consists of a reconfigurable illumination, DOEs, and an input layer. The reconfigurable illumination enables the switch between logical operations and casts light on the DOE cascade forming a DNN. In this paper, we focus on reconfigurable illumination with binary amplitude modulation and DOEs with phase modulation, assuming the use of commercially available optical components. We place the

two input images side by side on the input layer within the DOE cascade to achieve a simple optical setup. The output of the logic operation appears as an intensity distribution at the end of the cascade and is captured with an image sensor. The final result is binarized by assuming a one-bit image sensor or a computational process. The reconfigurable illumination and DOEs are specifically trained to perform the 16 SIMD logic operations on any two binary images, as detailed in the subsequent subsection. Once the training process is completed, DC enables massively parallel optical logic operations on arbitrary binary inputs just by selecting the illumination patterns, without necessitating any modifications to the DOEs.

2.2 Optical Forward Model

Figure 2 illustrates the forward and backward processes of DC. We consider a total L types of SIMD logic operations on N parallel bits. These operations are conducted by the optical cascade composed of K layers, including one illumination layer, one input layer, and $(K - 2)$ DOE layers, with the layer index denoted as $k \in \{1, 2, \dots, K\}$. The first layer of the optical cascade is the binary reconfigurable illumination $\mathbf{r}_l \in \{0, 1\}^{P_x \times P_y}$, where $l \in \{1, 2, \dots, L\}$ is the index of the logic operations. An input pair $\mathbf{f} \in \{0, 1\}^{N_x \times 2N_y}$, composed of side-by-side binary images, is located on the input layer, denoted as the K_{in} -th layer in the cascade.

Here, N_x and N_y represent the pixel counts of the individual images within the input pair along the x - and y -directions, respectively, where $N_x \times N_y = N$. The phase distributions for each DOE layer are denoted by $\phi_k \in \mathbb{R}^{P_x \times P_y}$, and P_x and P_y indicate the pixel counts of the DOEs along the x - and y -axes, respectively. The result of the logic operations is observed with the image sensor located downstream of the K -th layer in the optical cascade.

We describe below the forward process of DC. The complex amplitude modulation $\mathbf{v}_k \in$

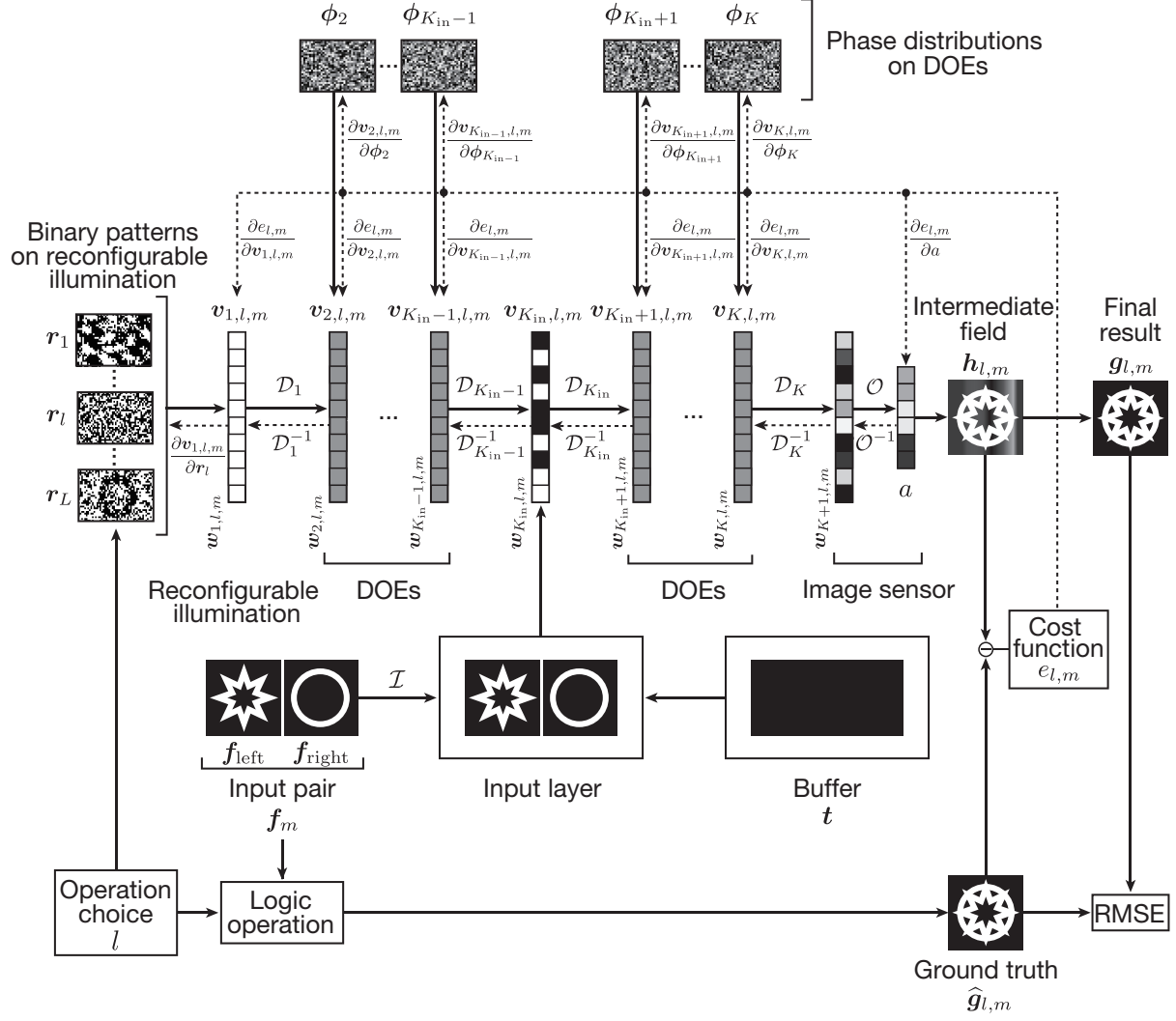


Fig 2 Forward and backward processes of DC. The reconfigurable illumination, the DOEs, and the scaling factor are optimized through the training process.

$\mathbb{C}^{P_x \times P_y}$, induced by the reconfigurable illumination, input pair, and the phase-only DOEs at the k -th layer in the cascade, is expressed as

$$\mathbf{v}_k = \begin{cases} \mathbf{r}_l & \text{for } k = 1, \\ \mathcal{I}[\mathbf{f}] + \mathbf{t} & \text{for } k = K_{\text{in}}, \\ \exp(j\phi_k) & \text{otherwise,} \end{cases} \quad (1)$$

$$\mathbf{v}_k = \begin{cases} \mathcal{I}[\mathbf{f}] + \mathbf{t} & \text{for } k = K_{\text{in}}, \\ \exp(j\phi_k) & \text{otherwise,} \end{cases} \quad (2)$$

$$\mathbf{v}_k = \begin{cases} \exp(j\phi_k) & \text{otherwise,} \end{cases} \quad (3)$$

where j denotes the imaginary unit. Here, \mathcal{I} is an operator transforming the input pair into an amplitude image on the input layer, composed of following two steps. The first step is up-sampling along the x - and y -directions with factors of $s_x \in \mathbb{N}$ and $s_y \in \mathbb{N}$, respectively. The second step is zero-padding to enlarge the up-sampled input pair to the DOE size ($P_x \times P_y$ pixels). $\mathbf{t} \in \{0, 1\}^{P_x \times P_y}$ expresses a buffer surrounding the up-sampled input pair as illustrated in Fig. 2 and is defined as follows:

$$\mathbf{t}(u_x, u_y) = \begin{cases} 0 & \text{for } \{u_x, u_y\} \in \left(\frac{P_x - s_x N_x}{2}, \frac{P_x + s_x N_x}{2} \right] \times \left(\frac{P_y - 2s_y N_y}{2}, \frac{P_y + 2s_y N_y}{2} \right], \\ 1 & \text{otherwise,} \end{cases} \quad (4)$$

$$\mathbf{t}(u_x, u_y) = \begin{cases} 1 & \text{otherwise,} \end{cases} \quad (5)$$

where $u_x \in \mathbb{N}$ and $u_y \in \mathbb{N}$ are indices along the x - and y -directions. This buffer is employed to compensate for light intensities transmitted or blocked on the input pair and enables the removal of computational encoding and decoding of the input and output, processes that are indispensably employed in previous optical logic operation methods, including the SC scheme.

The propagation process passing through the k -th layer in the cascade is written as

$$\mathbf{w}_{k+1} = \mathcal{D}_k[\mathbf{v}_k \mathbf{w}_k], \quad (6)$$

where $\mathbf{w}_k \in \mathbb{C}^{P_x \times P_y}$ is a complex amplitude field just before the k -th layer. \mathcal{D}_k is a diffraction operator representing the propagation from the k -th layer to the $(k + 1)$ -th layer, calculated based on the angular spectrum method.⁵² The initial field \mathbf{w}_1 is specified as an all-one matrix, indicating a uniform field at the start.

The output intensity field of the optical cascade is observed with the image sensor as follows:

$$\mathbf{h} = a\mathcal{O}[|\mathbf{w}_{K+1}|^2], \quad (7)$$

$$\mathbf{g} = \mathcal{B}[\mathbf{h}]. \quad (8)$$

Here, $\mathbf{h} \in \mathbb{R}^{P_x \times P_y}$ represents the intermediate field, obtained through an operator \mathcal{O} that first crops the central $s_x N_x \times s_y N_y$ pixels from the output intensity field and then down-samples it to the original input image size of $N_x \times N_y$. This process includes scaling the intensity by a factor of $a \in \mathbb{R}_{>0}$, which corresponds to either amplifying or attenuating the signal. $\mathbf{g} \in \mathbb{R}^{N_x \times N_y}$ is the final result of the logic operation, with the binarization operator \mathcal{B} defined as

$$\mathcal{B}[z] = \begin{cases} 0 & \text{for } z < 0.5, \\ 1 & \text{for } z \geq 0.5, \end{cases} \quad (9)$$

$$(10)$$

where $z \in \mathbb{R}$ is an arbitrary variable. The binarization process, which converts analog signals to boolean ones, is implemented using either a one-bit image sensor or through computational means.

2.3 Optimization Process

To realize optical logic operations in parallel, the illumination \mathbf{r}_l , the DOEs ϕ_k , and the scaling factor a are optimized based on gradient descent in this study. First, we describe the optimization process by assuming a single logic operation ($L = 1$) and a single input pair for simplicity, where

the illumination is defined as $\mathbf{r}_{L=1}$. Then, we extend the optimization process to arbitrary numbers of logic operations and input pairs.

2.3.1 Derivatives for a single logic operation and a single input pair

We define a cost function e for a single logic operation and a single input pair as follows:

$$e = \frac{1}{N} \sum_{\forall} |\mathbf{e}|^2, \quad (11)$$

where \sum_{\forall} represents the summation of all the elements of a tensor on its right side. Here, the error e is defined by

$$\mathbf{e} = \mathbf{h} - \hat{\mathbf{g}}, \quad (12)$$

which represents the difference between the intermediate field \mathbf{h} and the ground truth of the operation result $\hat{\mathbf{g}}$. This is to avoid the intermediate field's signals around the threshold values in \mathcal{B} , ensuring a robust binarization process.

To optimize $\mathbf{r}_{L=1}$ and ϕ_k based on gradient descent, the partial derivatives of e with respect to these variables are expressed by employing the chain rule as follows:

$$\frac{\partial e}{\partial \mathbf{r}_{L=1}} = \frac{\partial \mathbf{v}_1}{\partial \mathbf{r}_{L=1}} \cdot \frac{\partial e}{\partial \mathbf{v}_1}, \quad (13)$$

$$\frac{\partial e}{\partial \phi_k} = \frac{\partial \mathbf{v}_k}{\partial \phi_k} \cdot \frac{\partial e}{\partial \mathbf{v}_k}. \quad (14)$$

The right sides of these three partial derivatives include the partial derivative of e with respect to

\mathbf{v}_k , calculated as:

$$\frac{\partial e}{\partial \mathbf{v}_k} = \frac{4a}{N} \mathbf{w}_k^* \mathcal{D}_k^{-1} [\mathbf{v}_{k+1}^* \mathcal{D}_{k+1}^{-1} [\cdots [\mathbf{v}_K^* \mathcal{D}_K^{-1} [\mathbf{w}_{K+1} \mathcal{O}^{-1}[\mathbf{e}]]] \cdots]], \quad (15)$$

where \mathcal{D}_k^{-1} and \mathcal{O}^{-1} are operators representing the inverse processes of \mathcal{D}_k and \mathcal{O} , respectively, and the superscript $*$ denotes the complex conjugate.

The partial derivatives with respect to each optimized variable are finally written as follows:

The partial derivative with respect to $\mathbf{r}_{L=1}$ is described as

$$\frac{\partial e}{\partial \mathbf{r}_{L=1}} = \text{Re} \left[\frac{\partial e}{\partial \mathbf{v}_1} \right], \quad (16)$$

where $\text{Re}[\bullet]$ denotes the real part of a complex amplitude. The partial derivative with respect to ϕ_k is described as

$$\frac{\partial e}{\partial \phi_k} = \text{Re} \left[-j \mathbf{v}_k^* \frac{\partial e}{\partial \mathbf{v}_k} \right]. \quad (17)$$

The partial derivative with respect to a is described as

$$\frac{\partial e}{\partial a} = \frac{2}{aN} \sum_{\forall} h e. \quad (18)$$

2.3.2 Derivatives for multiple logic operations and multiple input pairs

Next, we extend the optimization process from a single logic operation and a single input pair as described above, to L logic operations and M input pairs. In this scenario, the cost function E is expressed as

$$E = \frac{1}{LM} \sum_{l,m} e_{l,m}, \quad (19)$$

where $e_{l,m}$ denotes the cost associated with the l -th logic operation and the m -th input pair, derived from Eq. (11). The partial derivatives of E with respect to \mathbf{r}_l , ϕ_k , and a are presented as summations of the partial derivatives of $e_{l,m}$ with respect to these variables, derived from Eqs. (16)–(18), respectively:

$$\frac{\partial E}{\partial \mathbf{r}_l} = \sum_m \frac{\partial e_{l,m}}{\partial \mathbf{r}_l}, \quad (20)$$

$$\frac{\partial E}{\partial \phi_k} = \sum_{l,m} \frac{\partial e_{l,m}}{\partial \phi_k}, \quad (21)$$

$$\frac{\partial E}{\partial a} = \sum_{l,m} \frac{\partial e_{l,m}}{\partial a}. \quad (22)$$

2.3.3 Updating procedure

The variables \mathbf{r}_l , ϕ_k , and a are updated with the partial derivatives in Eqs. (20)–(22) based on the Adam optimizer.⁵³ The updating processes for the DOEs ϕ_k and the scaling factor a are described as follows:

$$\phi_k \leftarrow \phi_k - \text{Adam} \left[\frac{\partial E}{\partial \phi_k} \right], \quad (23)$$

$$a \leftarrow a - \text{Adam} \left[\frac{\partial E}{\partial a} \right], \quad (24)$$

where $\text{Adam}[\cdot]$ represents an operator to calculate the updating step in the Adam optimizer with the derivatives. To simplify the physical realization of the illumination \mathbf{r}_l , we assume its binary implementations, such as digital micromirror devices, by introducing stochastic perturbations into

the gradient descent process.⁵⁴ The first step in the update process for the variables is as follows:

$$\tilde{\mathbf{r}}_l \leftarrow \mathcal{C} \left[\tilde{\mathbf{r}}_l - \text{Adam} \left[\frac{\partial E}{\partial \mathbf{r}_l} \right] \right], \quad (25)$$

where $\tilde{\mathbf{r}}_l$ is an intermediate variable for the backward process in the optimization of \mathbf{r}_l . Here, \mathcal{C} is an operator for clipping the range of values as follows:

$$\mathcal{C}[z] = \begin{cases} 0 & \text{for } z < 0, \\ 1 & \text{for } z > 1, \\ z & \text{otherwise.} \end{cases} \quad (26)$$

$$\mathcal{C}[z] = \begin{cases} 1 & \text{for } z > 1, \end{cases} \quad (27)$$

$$\mathcal{C}[z] = \begin{cases} z & \text{otherwise.} \end{cases} \quad (28)$$

Subsequently, \mathbf{r}_l in the forward process is updated as follows:

$$\mathbf{r}_l = \mathcal{B}[\tilde{\mathbf{r}}_l + \mathbf{q}]. \quad (29)$$

where $\mathbf{q} \in \mathbb{R}^{P_x \times P_y}$ is a uniform distribution between ± 0.5 , introduced to avoid local minima in the binary optimization. After the optimization process, \mathbf{r}_l is finalized as follows:

$$\mathbf{r}_l = \mathcal{B}[\tilde{\mathbf{r}}_l]. \quad (30)$$

3 Numerical Demonstration

3.1 Experimental Conditions

We numerically demonstrated DC with all sixteen logic operations ($L = 16$) for the boolean input pair of \mathbf{f}_{left} and $\mathbf{f}_{\text{right}}$, as shown in Tab. 1. In this numerical demonstration, the wavelength of the

Table 1 Logic operations defined on input pair.

| Input pair f_{left} f_{right} | Operation index l | Logic operation | Boolean |
|---|---------------------------|---|---------|
| | | | 0 0 1 1 |
| | | | 0 1 0 1 |
| Output \hat{g}_l | 1 | 0 | 0 0 0 0 |
| | 2 | $f_{\text{left}} \wedge f_{\text{right}}$ (AND) | 0 0 0 1 |
| | 3 | $f_{\text{left}} \wedge \overline{f_{\text{right}}}$ | 0 0 1 0 |
| | 4 | $\overline{f_{\text{left}}}$ | 0 0 1 1 |
| | 5 | $\overline{f_{\text{left}}} \wedge f_{\text{right}}$ | 0 1 0 0 |
| | 6 | f_{right} | 0 1 0 1 |
| | 7 | $f_{\text{left}} \oplus f_{\text{right}}$ (XOR) | 0 1 1 0 |
| | 8 | $f_{\text{left}} \vee f_{\text{right}}$ (OR) | 0 1 1 1 |
| | 9 | 1 | 1 1 1 1 |
| | 10 | $\overline{f_{\text{left}} \wedge f_{\text{right}}}$ (NAND) | 1 1 1 0 |
| | 11 | $\overline{f_{\text{left}} \vee f_{\text{right}}}$ | 1 1 0 1 |
| | 12 | $\overline{f_{\text{left}}}$ | 1 1 0 0 |
| | 13 | $f_{\text{left}} \vee \overline{f_{\text{right}}}$ | 1 0 1 1 |
| | 14 | $\overline{f_{\text{right}}}$ | 1 0 1 0 |
| | 15 | $\overline{f_{\text{left}} \oplus f_{\text{right}}}$ (XNOR) | 1 0 0 1 |
| | 16 | $\overline{f_{\text{left}} \vee f_{\text{right}}}$ (NOR) | 1 0 0 0 |

coherent light for the reconfigurable illumination λ was defined as $0.532 \mu\text{m}$. The optical cascade comprised eleven layers ($K = 11$), incorporating nine DOEs, with the input layer positioned as the sixth layer ($K_{\text{in}} = 6$). The intervals between the layers were equally set to $3 \times 10^4 \lambda$ ($\approx 1.60 \times 10^4 \mu\text{m}$). For the illumination pattern r_l , the DOEs ϕ_k , and the input layer, the pixel pitch was 16λ ($\approx 8.51 \mu\text{m}$), and the pixel count was 160 ($= P_x$) along the x -axis and 288 ($= P_y$) along the y -axis, respectively. For the input pair f_m , the pixel count of the individual image in the pair was 16 ($= N_x$) along the x -axis and 16 ($= N_y$) along the y -axis, where the parallel bits N became 256, and the up-sampling factors s_x and s_y were both 8, respectively. The width of the region with ones on the buffer t , as defined in Eq. (5), was set to 16 pixels. To prevent the circulant effect on the diffraction calculation, the complex amplitude fields were zero-padded with a width of 64 pixels during the layer-by-layer propagation processes.

For the optimization process, input pairs were generated with values initially selected from uniform random distributions between 0 and 1, and then binarized using randomly selected thresholds also between 0 and 1. The batch size M was set to 16 for training. The number of the iterations was 5000. The learning rates for the Adam optimizer, as used in Eqs. (23)–(25), for r_l , ϕ_k , and a were set to 3×10^{-2} , 1×10^{-2} , and 3×10^{-3} , respectively. These variables were initially set to uniform random distributions for r_l and ϕ_k , and 10 for a . The computation performance of DC was evaluated by the root mean squared errors (RMSEs) between the final result $g_{l,m}$ and the ground truth $\hat{g}_{l,m}$ for 256 randomly generated test input pairs.

3.2 Result

The optimization results for the illumination r_l and the DOEs ϕ_k are presented in Figs. 3(a) and 3(b), respectively. The scaling factor a was optimized to 23.8. Following this optimization, DC was numerically performed using an input pair with 256 parallel bits, which were not included in the training dataset, as shown in Fig. 4(a). Here, the sixteen SIMD logic operations were succeeded, as shown in Fig. 4(b). Moreover, the root mean squared errors (RMSEs) between the final result $g_{l,m}$ and the ground truth $\hat{g}_{l,m}$ for 256 randomly generated test input pairs were found to be 0. These outcomes underscore the promising potential for DC. More detailed discussions are provided in the subsequent section.

4 Comprehensive Analysis

We conducted a numerical analysis of the performance of DC under various optical conditions. This analysis evaluated the number of DOEs, the physical volume of DC, the position of the input layer, the energy efficiency, the buffer width, and the advantage of multiplexing operations.

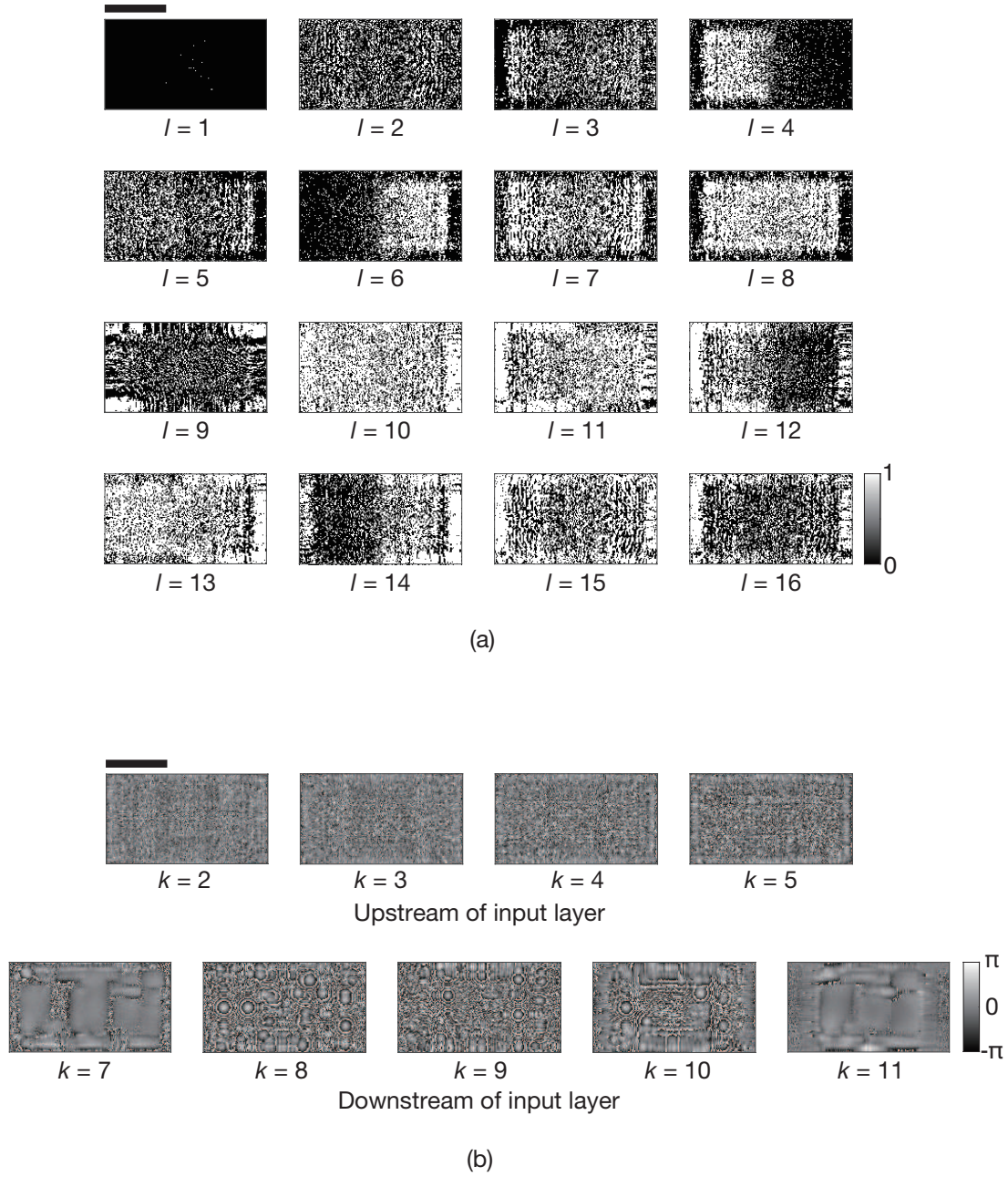


Fig 3 Optimization results. (a) Binary amplitude patterns on the reconfigurable illumination and (b) phase distributions on the DOEs. Scale bar is 1 mm.

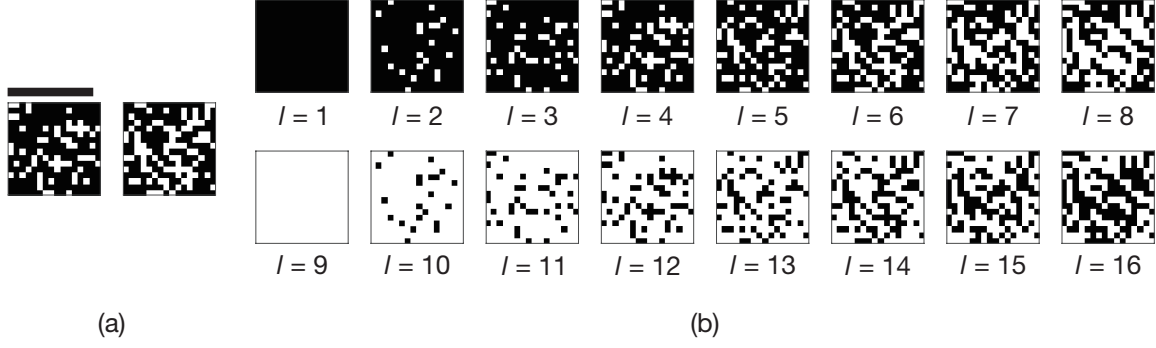


Fig 4 An example of the DC process with the optimized illumination and the DOEs shown in Fig. 3. (a) Input pair and (b) operation outputs. Scale bar is 1 mm, indicating the physical scale after the up-sampling process.

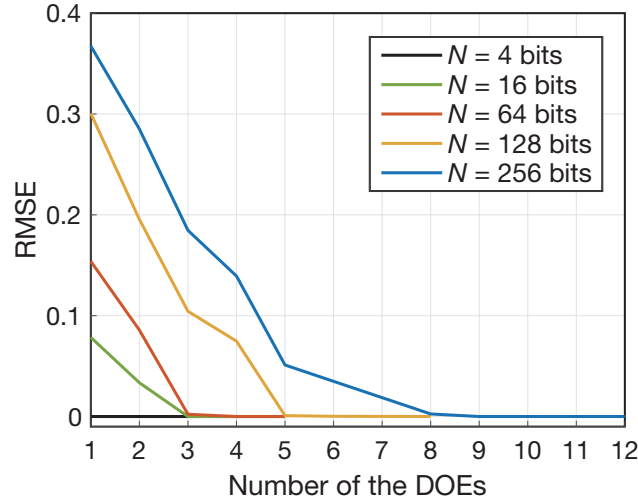


Fig 5 Computational errors associated with varying numbers of the DOEs.

Throughout this analysis, the experimental conditions were consistent with those described in Sec. 3, except where otherwise noted.

4.1 Number of the DOEs

The computational performance of DC, with the number of the DOEs set to $K - 2$, was evaluated using the RMSEs, as illustrated in Fig. 5. In this evaluation, the input parallel bits N were varied as 4, 16, 64, 128, and 256. Correspondingly, the up-sampling factors along x - and y -axis were adjusted to (64, 64), (32, 32), (16, 16), (8, 16), and (8, 8) ($= (s_x, s_y)$), respectively, aiming to

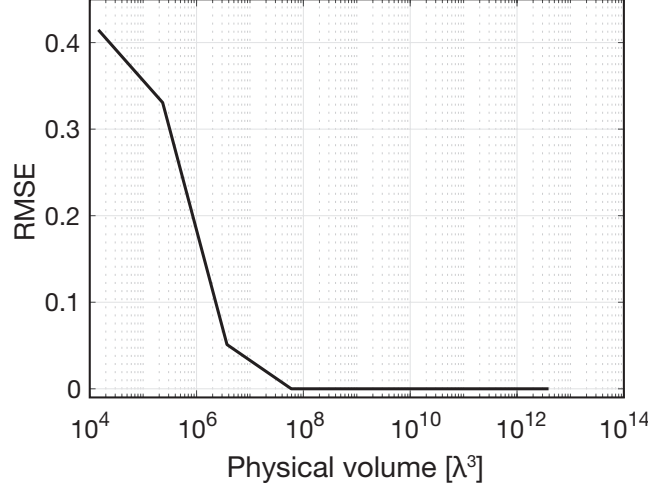


Fig 6 Computational errors associated with varying the physical volume of DC.

maintain consistent pixel counts 128 ($= s_x N_x, s_y N_y$) on the input layer after up-sampling. The layer index of the input layer K_{in} was set to $\lfloor (K - 2)/2 \rfloor + 2$.

As illustrated in Fig. 5, the calculation error decreased with an increase in the number of DOEs. Additionally, the necessary number of DOEs for achieving error-free calculation increased with the input parallel bits N , but at a rate less than proportional to N . This rate of increase was smaller than predicted in previous works,^{31,35} indicating an advantage of DC in terms of scalability and integration capability through the use of spatially parallelized optical processes for logic operations.

4.2 Physical Volume of DC

The physical volume of the optical cascade in Sec. 3.2 was calculated as $3.89 \times 10^{12} \lambda^3$ ($\approx 5.86 \times 10^{11} \mu\text{m}^3$), where the pixel pitch on the DOEs was 16λ and the intervals between the layers in the optical cascade were $3 \times 10^4 \lambda$, respectively. We investigated the computational error with respect to the reduction of the physical volume by scaling down both the pixel pitch and the interval with the same magnification ratio. The result is shown in Fig. 6. In this case, the minimal physical volume without computational error was $5.94 \times 10^7 \lambda^3$ ($\approx 8.94 \times 10^6 \mu\text{m}^3$), where the pixel pitch

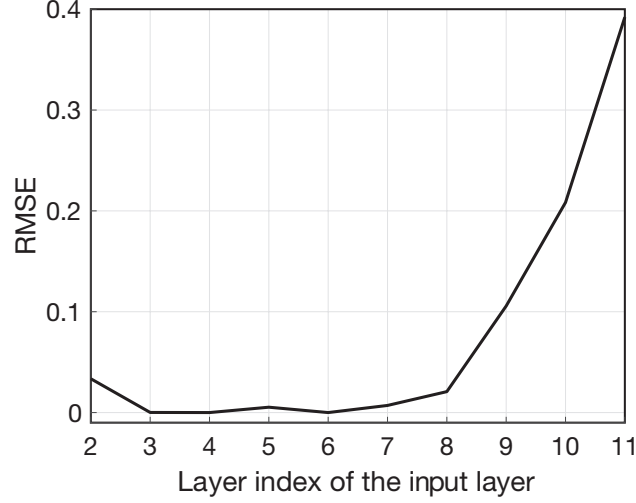


Fig 7 Computational errors under different positions of the input layer.

was λ ($= 0.532 \mu\text{m}$) and the interval was $1.17 \times 10^2 \lambda$ ($\approx 6.23 \times 10 \mu\text{m}$), respectively. This result indicated that the minimal physical volume of DC is constrained by the diffraction limit.

4.3 Position of the Input Layer

The computational error was calculated by varying the position of the input layer K_{in} from 2 to 11 in the optical cascade with 11 layers, as depicted in Fig. 7. This result shows the importance of the DOEs downstream from the input layer in reducing computational error. It suggests an advantage in positioning the input layer at an upper layer, excluding the top one.

4.4 Energy Efficiency

We evaluated the light energy efficiency of DC using the following definition:

$$\text{Energy efficiency} = \frac{\sum_{\forall} [\mathcal{O}[|\mathbf{w}_{K+1}|^2]]|_{l=9, \mathbf{f}=1}}{P_x P_y}. \quad (31)$$

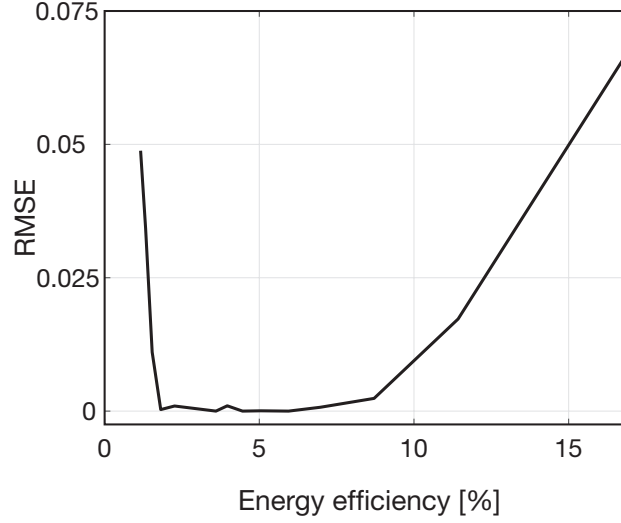


Fig 8 Relationship between computational errors and energy efficiencies when varying the scaling factor.

Here, the denominator represents the total input energy to the optical cascade. The numerator is the total energy on the output area of interest, calculated when the logic operation is configured to produce one output ($l = 9$) and all elements of the input pair \mathbf{f} are set to one. The energy efficiency was assessed with respect to the scaling factor a and the width of the buffer t .

4.4.1 Scaling factor

The light energy efficiency is associated with the scaling factor a , which amplifies or attenuates the signals captured by the image sensor before the binarization process. A larger a indicates lower energy efficiency and vice versa. In the above demonstrations and analyses, a was included in the optimized parameters, as shown in Eq. (24). Here, a was set to a specific value and was not updated during the optimization process. Once the optimizations of the illumination pattern \mathbf{r}_l and the DOEs ϕ_k were completed, the energy efficiency in Eq. (31) and the computational error were calculated. This process was repeated by changing a from 2 to 32. The relationship between the energy efficiency and the computational error is shown in Fig. 8. The RMSEs for the energy efficiencies between 1.81% and 8.71% were less than 2.38×10^{-3} . Therefore, nearly error-free

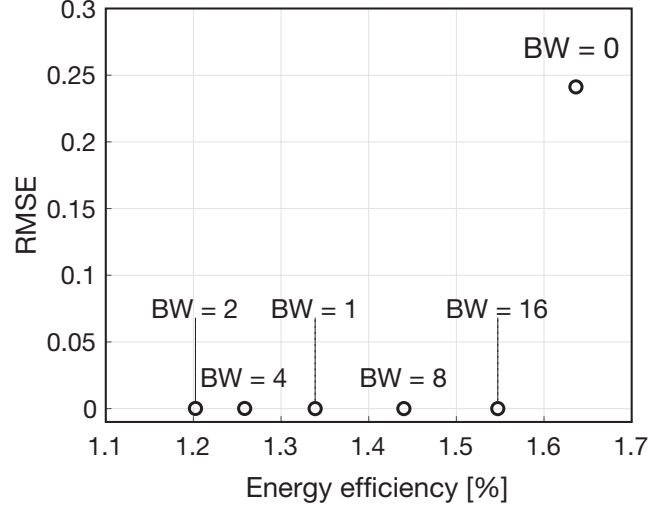


Fig 9 Relationship between computational errors and energy efficiencies with varying buffer widths (BW [pixels]).

calculation was achieved within this range of energy efficiencies.

The primary sources of energy loss were amplitude modulation on the illumination plane, light leakage from the optical cascade, and the cropping of the limited square area by the image sensor at the end of the optical cascade. The first issue can be solved by employing phase modulation on the illumination plane, although its modulation speed is lower than that of amplitude modulation on currently available spatial light modulators. The second issue may be alleviated by reducing the intervals between layers. The third issue can be addressed by increasing the sensor area, employing anisotropic sampling, or utilizing anamorphic imaging. Another approach to improve the energy efficiency is to increase the width of the buffer, as indicated in the next section.

4.4.2 Buffer width

The buffer t was introduced into DC to compensate for the light intensities transmitted or blocked by the input pair. It was expected to eliminate the computational encoding and decoding processes employed in previous methods for optical logic operations, including the SC scheme. In the above demonstrations and analyses, the buffer width was set to 16 pixels. The plots in Fig. 9 show the

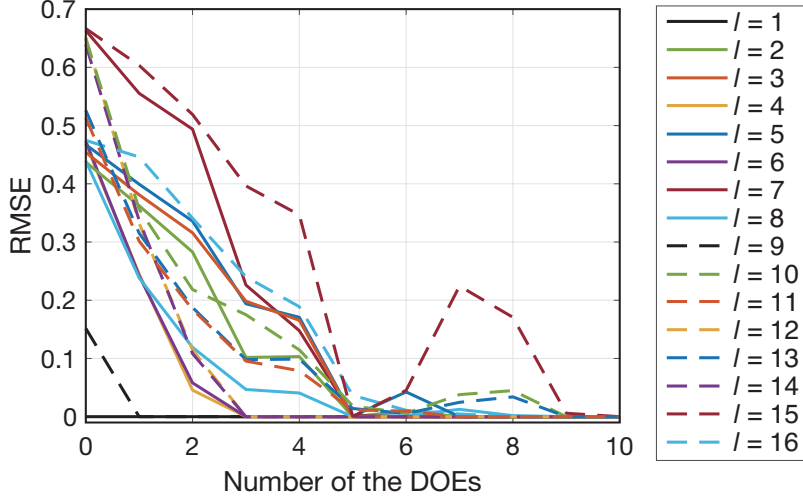


Fig 10 Computational errors associated with varying the number of DOEs for a single logic operation.

energy efficiencies and computational errors at different buffer widths, including zero width. In this analysis, the scaling factor a was included in the optimization parameters. This result supported the necessity of the buffer for error-free calculation. Furthermore, a larger buffer width increased energy efficiency.

The RMSE for the logic operations at $1 \leq l \leq 8$ without the buffer was reduced from 4.24×10^{-2} to 0 by adding a buffer of 1 pixel. On the other hand, the RMSE for the logic operations at $9 \leq l \leq 16$ with no buffer was significantly improved from 4.40×10^{-1} to 0 by adding a one-pixel buffer. As shown in Tab. 1, operations at $1 \leq l \leq 8$ do not include the operation with input of $f_{\text{left}} = 0, f_{\text{right}} = 0$ and output of $\hat{g}_l = 1$. Conversely, operations at $9 \leq l \leq 16$ include such an operation. This result also verified the role of the buffer—compensating for the balance between the light intensities of the input and output in the optical cascade.

4.5 Multiplexing Advantage

The DOEs in DC multiplexed 16 logic operations, as shown in Tab. 1. We confirmed the computational errors under different numbers of DOEs, denoted as $K - 2$, when the optical cascade

was designed for a single logic operation, as illustrated in Fig. 10. This highlights the benefits of multiplexing these operations. The layer index of the input layer, K_{in} , was set to $\lfloor (K - 2)/2 \rfloor + 2$. When the number of DOEs was zero, only the illumination pattern was optimized for each logic operation. In most cases, error-free calculations for single logic operations were achieved when the number of DOEs was larger than 6. On the other hand, as shown in Fig. 5, the necessary number of DOEs for multiplexing 16 logic operations was 9, which is significantly less than 6×16 . This result verified the multiplexing advantage and the integration capability of DC.

5 Conclusion

We revived SC as DC by employing DNNs to achieve scalable and flexible optical SIMD operations. The optical cascade of DC consisted of reconfigurable illumination, DOEs, and an input layer. The illumination patterns and DOEs were designed to perform 16 logic operations on any binary input image pairs, and the output intensity of the optical cascade was binarized to produce the final results. The advantages of DC included scalability, integration capability, and all-optical operation without the need for computational encoding and decoding, all of which were numerically demonstrated.

An issue with DC for practical applications is its low energy efficiency. This may be addressed by adopting illumination with phase modulation and optimizing physical conditions, including the layer interval, buffer, and image sensor. DC is extendable to a versatile mode of input and operation beyond the SIMD logic operations, owing to its flexible architecture and learning-based approach. Furthermore, incorporating multiplexing in various optical quantities, such as time,^{55,56} wavelength,⁵⁷ polarization,^{36,58} and orbital angular momentum³⁹ would enhance the computational capacity in DC. Thus, our study on DC offers a novel design architecture for optical computers and

optical accelerators, and paves the way for a next-generation optical computing paradigm.

Disclosures

The authors declare no conflicts of interest.

Code and Data Availability

Data may be obtained from the authors upon reasonable request.

References

- 1 G. E. Moore, “Cramming more components onto integrated circuits,” *Proceedings of IEEE* **86**(1), 82–85 (1998).
- 2 H. J. Caulfield and S. Dolev, “Why future supercomputing requires optics,” *Nature Photonics* **4**(5), 261–263 (2010).
- 3 K. Kitayama, M. Notomi, M. Naruse, *et al.*, “Novel frontier of photonics for data processing—photonic accelerator,” *APL Photonics* **4**(9), 1–25 (2019).
- 4 J. W. Goodman, A. Dias, and L. Woody, “Fully parallel, high-speed incoherent optical method for performing discrete Fourier transforms,” *Optics Letters* **2**(1), 1–3 (1978).
- 5 R. P. Bocker, “Matrix multiplication using incoherent optical techniques,” *Applied Optics* **13**(7), 1670–1676 (1974).
- 6 R. A. Athale and W. C. Collins, “Optical matrix–matrix multiplier based on outer product decomposition,” *Applied Optics* **21**(12), 2089–2090 (1982).
- 7 M. Gruber, J. Jahns, and S. Sinzinger, “Planar-integrated optical vector-matrix multiplier,” *Applied Optics* **39**(29), 5367–5373 (2000).

- 8 Y. Owechko, G. J. Dunning, E. Marom, *et al.*, “Holographic associative memory with nonlinearities in the correlation domain,” *Applied Optics* **26**(10), 1900–1910 (1987).
- 9 E. G. Paek and D. Psaltis, “Optical associative memory using Fourier transform holograms,” *Optical Engineering* **26**(5), 428–433 (1987).
- 10 M. Ishikawa, N. Mukohzaka, H. Toyoda, *et al.*, “Optical associatron: a simple model for optical associative memory,” *Applied Optics* **28**(2), 291–301 (1989).
- 11 J. Tanida and Y. Ichioka, “Optical logic array processor using shadowgrams,” *The Journal of the Optical Society of America* **73**(6), 800–809 (1983).
- 12 Y. Ichioka and J. Tanida, “Optical parallel logic gates using a shadow-casting system for optical digital computing,” *Proceedings of the IEEE* **72**(7), 787–801 (1984).
- 13 J. Tanida and Y. Ichioka, “OPALS: optical parallel array logic system,” *Applied Optics* **25**(10), 1565–1570 (1986).
- 14 K.-H. Brenner, A. Huang, and N. Streibl, “Digital optical computing with symbolic substitution,” *Applied Optics* **25**(18), 3054–3060 (1986).
- 15 D. A. Miller, “Self-configuring universal linear optical component,” *Photonics Research* **1**(1), 1–15 (2013).
- 16 Y. Shen, N. C. Harris, S. Skirlo, *et al.*, “Deep learning with coherent nanophotonic circuits,” *Nature Photonics* **11**(7), 441–446 (2017).
- 17 N. C. Harris, J. Carolan, D. Bunandar, *et al.*, “Linear programmable nanophotonic processors,” *Optica* **5**(12), 1623–1631 (2018).
- 18 M. Zhang, L. Wang, and P. Ye, “All optical XOR logic gates: technologies and experiment demonstrations,” *IEEE Communications Magazine* **43**(5), S19–S24 (2005).

- 19 Y. Zhang, Y. Zhang, and B. Li, “Optical switches and logic gates based on self-collimated beams in two-dimensional photonic crystals,” *Optics Express* **15**(15), 9287–9292 (2007).
- 20 Y.-D. Wu, T.-T. Shih, and M.-H. Chen, “New all-optical logic gates based on the local non-linear Mach-Zehnder interferometer,” *Optics Express* **16**(1), 248–257 (2008).
- 21 K.-S. Lee and S.-K. Kim, “Conceptual design of spin wave logic gates based on a Mach-Zehnder-type spin wave interferometer for universal logic functions,” *Journal of Applied Physics* **104**(053909), 1–5 (2008).
- 22 J. Dong, X. Zhang, and D. Huang, “A proposal for two-input arbitrary Boolean logic gates using single semiconductor optical amplifier by picosecond pulse injection,” *Optics Express* **17**(10), 7725–7730 (2009).
- 23 Y. Fu, X. Hu, and Q. Gong, “Silicon photonic crystal all-optical logic gates,” *Physics Letters A* **377**(3-4), 329–333 (2013).
- 24 D. G. Sankar Rao, S. Swarnakar, and S. Kumar, “Performance analysis of all-optical NAND, NOR, and XNOR logic gates using photonic crystal waveguide for optical computing applications,” *Optical Engineering* **59**(5), 057101–057101 (2020).
- 25 Y. Xie, Z. Geng, L. Zhuang, *et al.*, “Programmable optical processor chips: toward photonic RF filters with DSP-level flexibility and MHz-band selectivity,” *Nanophotonics* **7**(2), 421–454 (2017).
- 26 W. Bogaerts, D. Pérez, J. Capmany, *et al.*, “Programmable photonic circuits,” *Nature* **586**(7828), 207–216 (2020).
- 27 Z. Ying, C. Feng, Z. Zhao, *et al.*, “Electronic-photonic arithmetic logic unit for high-speed computing,” *Nature Communications* **11**(2154), 1–9 (2020).

- 28 X. Lin, Y. Rivenson, N. T. Yardimci, *et al.*, “All-optical machine learning using diffractive deep neural networks,” *Science* **361**(6406), 1004–1008 (2018).
- 29 T. Yan, J. Wu, T. Zhou, *et al.*, “Fourier-space diffractive deep neural network,” *Physical Review Letters* **123**(023901), 1–6 (2019).
- 30 H. Chen, J. Feng, M. Jiang, *et al.*, “Diffractive deep neural networks at visible wavelengths,” *Engineering* **7**(10), 1483–1491 (2021).
- 31 H. Zhu, J. Zou, H. Zhang, *et al.*, “Space-efficient optical computing with an integrated chip diffractive neural network,” *Nature Communications* **13**(1044), 1–9 (2022).
- 32 Y. Luo, Y. Zhao, J. Li, *et al.*, “Computational imaging without a computer: seeing through random diffusers at the speed of light,” *Elight* **2**(4), 1–16 (2022).
- 33 Ç. Işıl, D. Mengü, Y. Zhao, *et al.*, “Super-resolution image display using diffractive decoders,” *Science Advances* **8**(eadd3433), 1–17 (2022).
- 34 T. Igarashi, M. Naruse, and R. Horisaki, “Incoherent diffractive optical elements for extendable field-of-view imaging,” *Optics Express* **31**(19), 31369–31382 (2023).
- 35 O. Kulce, D. Mengü, Y. Rivenson, *et al.*, “All-optical information-processing capacity of diffractive surfaces,” *Light: Science & Applications* **10**(25), 1–17 (2021).
- 36 J. Li, Y.-C. Hung, O. Kulce, *et al.*, “Polarization multiplexed diffractive computing: all-optical implementation of a group of linear transformations through a polarization-encoded diffractive network,” *Light: Science & Applications* **11**(153), 1–20 (2022).
- 37 J. Li, T. Gan, B. Bai, *et al.*, “Massively parallel universal linear transformations using a wavelength-multiplexed diffractive optical network,” *Advanced Photonics* **5**(016003), 1–23 (2023).

- 38 C. Qian, X. Lin, X. Lin, *et al.*, “Performing optical logic operations by a diffractive neural network,” *Light: Science & Applications* **9**(59), 1–7 (2020).
- 39 P. Wang, W. Xiong, Z. Huang, *et al.*, “Orbital angular momentum mode logical operation using optical diffractive neural network,” *Photonics Research* **9**(10), 2116–2124 (2021).
- 40 S. Zarei and A. Khavasi, “Realization of optical logic gates using on-chip diffractive optical neural networks,” *Scientific Reports* **12**(15747), 1–13 (2022).
- 41 Y. Luo, D. Mengu, and A. Ozcan, “Cascadable all-optical NAND gates using diffractive networks,” *Scientific Reports* **12**(7121), 1–11 (2022).
- 42 X. Liu, D. Zhang, L. Wang, *et al.*, “Parallelized and cascadable optical logic operations by few-layer diffractive optical neural network,” in *Photonics*, **10**(5), 503:1–503:7 (2023).
- 43 M. Sonka, V. Hlavac, and R. Boyle, *Image processing, analysis and machine vision*, Springer (2013).
- 44 J. A. Dev, “Bitcoin mining acceleration and performance quantification,” in *2014 IEEE 27th Canadian Conference on Electrical and Computer Engineering (CCECE)*, 1–6, IEEE (2014).
- 45 A. Reuther, P. Michaleas, M. Jones, *et al.*, “Survey and benchmarking of machine learning accelerators,” in *2019 IEEE High Performance Extreme Computing Conference (HPEC)*, 1–9, IEEE (2019).
- 46 J. D. Owens, M. Houston, D. Luebke, *et al.*, “GPU computing,” *Proceedings of IEEE* **96**(5), 879–899 (2008).
- 47 N. P. Jouppi, C. Young, N. Patil, *et al.*, “In-datacenter performance analysis of a tensor processing unit,” in *Proceedings of the 44th Annual International Symposium on Computer Architecture*, 1–12 (2017).

- 48 J. Rose, A. El Gamal, and A. Sangiovanni-Vincentelli, “Architecture of field-programmable gate arrays,” *Proceedings of the IEEE* **81**(7), 1013–1029 (1993).
- 49 X. Zhang, A. Ramachandran, C. Zhuge, *et al.*, “Machine learning on FPGAs to face the IoT revolution,” in *2017 IEEE/ACM International Conference on Computer-Aided Design (ICCAD)*, 894–901 (2017).
- 50 K. R. Hari, S. Y. Sai, *et al.*, “Cryptocurrency mining–transition to cloud,” *International Journal of Advanced Computer Science and Applications* **6**(9), 1–11 (2015).
- 51 E. Nurvitadhi, J. Sim, D. Sheffield, *et al.*, “Accelerating recurrent neural networks in analytics servers: Comparison of FPGA, CPU, GPU, and ASIC,” in *2016 26th International Conference on Field Programmable Logic and Applications (FPL)*, 1–4 (2016).
- 52 J. W. Goodman, *Introduction to Fourier optics*, Roberts and Company publishers (2005).
- 53 D. P. Kingma and J. Ba, “Adam: A method for stochastic optimization,” *ArXiv Preprint ArXiv:1412.6980*, 1–15 (2014).
- 54 M. Courbariaux, Y. Bengio, and J.-P. David, “Binaryconnect: Training deep neural networks with binary weights during propagations,” *Advances in Neural Information Processing Systems* **28**, 1–9 (2015).
- 55 Z. Zhang, F. Feng, J. Gan, *et al.*, “Space-time projection enabled ultrafast all-optical diffractive neural network,” *Laser & Photonics Reviews* **2301367**, 1–9 (2024).
- 56 J. Zhou, H. Pu, and J. Yan, “Spatiotemporal diffractive deep neural networks,” *Optics Express* **32**(2), 1864–1877 (2024).
- 57 Z. Duan, H. Chen, and X. Lin, “Optical multi-task learning using multi-wavelength diffractive deep neural networks,” *Nanophotonics* **12**(5), 893–903 (2023).

- 58 X. Luo, Y. Hu, X. Ou, *et al.*, “Metasurface-enabled on-chip multiplexed diffractive neural networks in the visible,” *Light: Science & Applications* **11**(158), 1–11 (2022).